Research Square

Preprints are preliminary reports that have not undergone peer review.
They should not be considered conclusive, used to inform clinical practice,
or referenced by the media as validated information.

Colossal liquid-state barocaloric Effect

Peng Tong

tongpeng@issp.ac.cn

Institute of Solid State Physics, HFIPS, Chinese Academy of Sciences https://orcid.org/0000-0003-3609-6190

Tingjiao Xiong

Key Laboratory of Materials Physics, Institute of Solid State Physics, Chinese Academy of Sciences

Keke Liu

Institute of Solid State Physics, HFIPS, Chinese Academy of Sciences

Jianchao Lin

Institute of Solid State Physics, Chinese Academy of Sciences https://orcid.org/0000-0003-4826-3080

Yongsheng Zhang

Qufu Normal University https://orcid.org/0000-0003-0007-0589

Xiaobing Liu

Qufu Normal University https://orcid.org/0000-0002-0680-1947

Dehong Yu

Australian Nuclear Science and Technology Organization https://orcid.org/0000-0003-2995-0336

Runjian Jiang

Institute of Solid State Physics, Chinese Academy of Sciences

Zhikang Liu

Institute of Solid State Physics, HFIPS, Chinese Academy of Sciences

Kun Zhang

Shenyang National Laboratory for Materials Science https://orcid.org/0000-0002-6290-2080

Yifang Liu

Institute of Metals Research CAS

Bing Li

Institute of Metals Research CAS https://orcid.org/0000-0002-0132-5021

Bao Yuan

IHEP, CAS

Wenhai Song

Institute of Solid State Physics, Chinese Academy of Sciences

Yuping Sun

Institute of Solid State Physics Chinese Academy of Sciences Hefei https://orcid.org/0000-0003-2477-285X

Physical Sciences - Article

Keywords:

Posted Date: November 11th, 2026

DOI: https://doi.org/10.21203/rs.3.rs-10849573/v1

License: This work is licensed under a Creative Commons Attribution 4.0 International License. Read Full License

Additional Declarations: There is **NO** Competing Interest.

Colossal liquid-state barocaloric Effect

Tingjiao Xiong[1,2,10], Keke Liu[1,2,10], Jianchao Lin[1,2,*], Yongsheng Zhang[3,4,*], Xiaobing Liu[3,4], Dehong Yu[5,*], Runjian Jiang[1,2], Zhikang Liu[1,2], Kun Zhang[6], Yifang Liu[6], Bing Li[6], Bao Yuan[7], Wenhai Song[1,2], Yuping Sun[1,8,9], Peng Tong[1,2,*]

[1]*Key Laboratory of Materials Physics, Institute of Solid State Physics, HFIPS, Chinese Academy of Sciences, Hefei 230031, China*

[2] *University of Science and Technology of China, Hefei 230026, China*

[3] *Key Laboratory of Quantum Materials under Extreme Conditions in Shandong Province, School of Physics and Physical Engineering, Qufu Normal University, Qufu 273165, China.*

[4] *Laboratory of High Pressure Physics and Material Science (HPPMS), Advanced Research Institute of Multidisciplinary Sciences, Qufu Normal University, Qufu 273165, China.*

[5] *Australian Nuclear Science and Technology Organisation, Lucas Heights, NSW 2234, Australia*

[6] *Shenyang National Laboratory for Materials Science, Institute of Metal Research, Chinese Academy of Sciences, Shenyang, China.*

[7] *Spallation Neutron Source Science Center, Institute of High Energy Physics, Chinese Academy of Sciences, Dongguan 523803, China*

[8] *Anhui Provincial Key Laboratory of Low-Energy Quantum Materials and Devices, High Magnetic Field Laboratory, HFIPS, Chinese Academy of Sciences, Hefei 230031, China*

[9] *Collaborative Innovation Center of Advanced Microstructures, Nanjing University, Nanjing 210093, China*

[10] *These authors contributed equally to this work.*

[*]Corresponding authors: jclin@issp.ac.cn; yshzhang@qfnu.edu.cn; dyu@ansto.gov.au; tongpeng@issp.ac.cn

Vapor-compression refrigeration, though ubiquitous, relies on gaseous refrigerants with substantial climate footprints. Solid-state caloric (SSC) cooling offers a green alternative, yet its performance is constrained by field hysteresis and parasitic losses from secondary-fluid heat exchange. Here we demonstrate the

liquid-state barocaloric effect in molecular liquids, achieving isothermal entropy changes of 230 $J \cdot kg^{-1} \cdot K^{-1}$ and adiabatic temperature changes of 32 K. Without requiring a liquid-solid transition, the liquid-state BC effect is robust over a temperature span exceeding 100 K. Together with the colossal entropy change, this leads to a relative cooling power three times that of SSC materials. Crucially, the liquid serves simultaneously as refrigerant, heat-transfer medium, and pressure-transmitting fluid, eliminating interfacial thermal resistance and enabling a Carnot-like cycle with a coefficient of performance far surpassing that of SSC systems. Molecular dynamics simulations and quasi-elastic neutron scattering reveal that the colossal thermal response originates from pressure-suppressed translational and rotational molecular motions, primarily governed by molecular polarity and intermolecular interactions. Our work establishes liquid-state barocaloric cooling as a sustainable paradigm that circumvents the longstanding efficiency bottlenecks of SSC refrigeration.

Introduction

Vapor-compression refrigeration (VCR), first conceived in 1805[1], has become indispensable in modern society, serving applications ranging from food preservation and thermal comfort to industrial processing and biomedical storage[2]. Yet current VCR systems predominantly rely on hydrofluorocarbon refrigerants, which have high global-warming potentials (GWP)[3]. The Kigali Amendment now mandates the phase-down of these gases[3], spurring both the search for zero-GWP alternatives and the development of entirely new cooling technologies based on non-gas refrigerants[4-9].

Solid-state caloric (SSC) cooling has attracted considerable interest as a promising new route that exploits the thermal response of solids to external fields[6]. SSC effects are classified as magnetocaloric (MC)[10], electrocaloric (EC)[11,12], elastocaloric (eC)[13], or barocaloric (BC)[5], depending on the applied field (magnetic, electric, uniaxial stress, or hydrostatic pressure). Recently, colossal SSC effects with entropy changes $|\Delta S|$ exceeding 100 $J \cdot kg^{-1} \cdot K^{-1}$ have been reported in plastic crystals[14-16], hybrid perovskites[17,18], spin-crossover compounds[19], charge-transfer solids[20] and high-entropy

polymers[11]. However, these colossal thermal responses almost invariably arise from field-driven first-order phase transitions, which entail substantial hysteresis[4,5]. Such hysteresis not only demands stronger fields for cyclic reversibility but also narrows the usable temperature window[4,5]. Moreover, SSC systems typically require a separate heat-transfer fluid to exchange heat between solid refrigerant and target environment[7,9,21]. These factors collectively degrade cooling performance and energy efficiency[22]. Pressure-induced liquid-solid phase transitions also exhibit colossal BC effects, sometimes even surpassing those of SSC materials, yet they suffer from the same drawbacks[23].

Here we explore the BC effect in the "pure" liquid state of molecular liquids. Without pressure-induced solidification, the entropy change increases continuously with pressure and remains robust over a temperature span exceeding 100 K. At 300 MPa, we observed a colossal $|\Delta S|$ of over 230 $J \cdot kg^{-1} \cdot K^{-1}$ and an adiabatic temperature change $|T_{ad}|$ greater than 30 K. Such colossal BC effects arise from pressure-suppressed translational and rotational motions of the molecules, the details of which depend on intermolecular interactions governed by molecular polarity. More importantly, the absence of hysteresis and the elimination of heat-exchange fluids enables a Carnot-like cycle, which approaches the Carnot efficiency limit. Our findings establish liquid-state BC cooling as a fundamentally distinct and highly efficient refrigeration paradigm, diverging from both conventional VCR and existing SSC technologies.

Concept of liquid-state BC refrigeration

Because liquid molecules have relatively weak intermolecular interactions, they can diffuse and rotate, leading to high entropy[24, 25]. Applying pressure strengthens molecular interactions and confines motional degrees of freedom, so a considerable entropy reduction is anticipated[24] (**Fig. 1a**). Upon depressurization, these constraints are released, restoring high molecular mobility and entropy. Because this entropy modulation does not involve a liquid-solid phase transition and thus is continuous, it inherently avoids the pronounced hysteresis that characterizes SSC materials (**Fig. 1b**). The hysteresis-free nature ensures that the entropy change is reversible over cyclic operation, eliminating internal dissipative losses. At the same time, the liquid refrigerant can serve as the heat-transfer fluid, eliminating the need for a secondary heat-exchange loop, a main source of external irreversibility unavoidable in SSC systems. Therefore, for liquid-state BC refrigeration, the coefficient of performance

(COP) and energy efficiency are fundamentally superior to those of SSC approaches, and the system would follow a Carnot-like refrigeration cycle (**Fig. 1c**).

Liquid-state barocaloric effects in over twenty molecular liquids

To materialize this concept, we selected over twenty molecular liquids with molecular weights ranging from 32 to 116 $g \cdot mol^{-1}$. This selection covers three representative categories of intermolecular interactions: dispersion-dominated (e.g., n-alkanes), dipole-dominated (e.g., esters, ketones, and nitriles), and hydrogen-bonding (HB)-dominated (e.g., alcohols, amines, and carboxylic acids). $|\Delta T_{ad}|$ was measured for all 23 liquids at pressures up to 300 MPa (Supplementary Fig. S1 to Fig. S22). Their solidification temperatures are sufficiently low that the pressure required to induce a liquid-solid transition far exceeds the applied range. For ethyl acetate, as an example, no solidification is observed even under 600 MPa at room temperature (**Extended Data Fig. 1**).

The measured $|\Delta T_{ad}|$ and derived $|\Delta S|$ values at various temperatures and pressures are compiled in **Extended Data Fig. 2** (see Methods and Supplementary Fig. S23 and Table S1 for data reduction). The seven liquids with the largest $|\Delta T_{ad}|$ and the seven with the largest $|\Delta S|$ are plotted in **Fig. 2a** and **Fig. 2b**, respectively. At 300 K, acetone, acetonitrile, n-hexane, methyl formate, propionaldehyde, and butyraldehyde concurrently exhibit $|\Delta T_{ad}|$ larger than 13 K and $|\Delta S|$ larger than 85 $J \cdot kg^{-1} \cdot K^{-1}$ at 100 MPa. Both quantities rise steeply with increasing pressure and temperature. At 320 K and 300 MPa, n-hexane, acetone and acetonitrile yield $|\Delta T_{ad}|$ exceeding 32 K and $|\Delta S|$ above 230 $J \cdot kg^{-1} \cdot K^{-1}$, rivaling the best values reported for colossal BC materials based on solid-state or liquid-solid transitions[14,17-20,23].

A defining advantage of liquid-state BC refrigeration is its exceptionally wide operating temperature range, from the solidification temperature to the boiling temperature, typically exceeding 100 K. To capture this feature, we evaluate the relative cooling power (RCP)[4,17] by integrating $|\Delta S|$ over the working temperature span (Supplementary Fig. S24). RCP measures the heat extracted per refrigeration cycle and is an important refrigeration metric. Half of the tested liquids (e.g., n-hexane, ethyl acetate, 1,3-butanediol, acetone, etc.) exhibit a colossal RCP of $1.3\text{-}1.8\times10^4$ $J \cdot kg^{-1}$, which is more than 3 times higher than that of typical SSC materials ($<0.4\times10^4$ $J \cdot kg^{-1}$), and about two times higher than those based on liquid-solid transition (e.g., 1×10^4 $J \cdot kg^{-1}$ for n-hexadecane) (**Fig. 2c**). Full data are listed in **Extended Data Table 1**.

Performance of Carnot-like liquid-state BC refrigeration

The good reversibility and the absence of a secondary heat-transfer fluid allow liquid-state BC refrigeration to adopt a Carnot-like cycle[7] (**Extended Data Fig. 3**). Under standard air-conditioner operating conditions (cold reservoir and heat-sink temperatures of 300 K and 308 K, respectively)[7], the COP approaches the Carnot limit of 37.5. **Fig. 2d** and **Extended Data Table 2** compare the COP, $|\Delta T_{ad}|$ and reversible $|\Delta S|$ ($|\Delta S_{rev}|$) of liquid-state BC refrigeration with those of typical SSC and emerging liquid-state dipolar-caloric and resolution-BC refrigeration. The liquid-state BC approach shows clear advantages over conventional SSC refrigeration, and outperforms dipolar-caloric[9] and dissolution-BC[7] alternatives in both COP and $|\Delta T_{ad}|$. The per-cycle cooling capacities of the BC cycle operated at 300 MPa are 65 $J \cdot g^{-1}$ for n-hexane and 80 $J \cdot g^{-1}$ for ethyl acetate (**Extended Data Fig. 3**), comparable to those reported recently in the dissolution-BC refrigeration cycle based on NH_4SCN aqueous solutions (67 $J \cdot g^{-1}$ at 600 MPa)[7]. Moreover, the liquids are free from the mechanical fatigue and durability concerns that plague solid refrigerants[5]. Indeed, the liquid-state BC effect of ethyl acetate didn't show visible degradation after 20 cycles between 0.1 and 100 MPa (**Extended Data Fig. 4**).

Dynamics from quasi-elastic neutron scattering

To reveal the dynamics of liquids at the atomic or molecular level, Quasi-elastic neutron scattering (QENS) was measured for n-hexane, ethyl acetate, and 1,3-butanediol, which have nearly similar molecular weights (~90 g/mol), but remarkably different $|\Delta S|$ values at 100 MPa, i.e., 113 $J \cdot kg^{-1} \cdot K^{-1}$, 91 $J \cdot kg^{-1} \cdot K^{-1}$, and 63 $J \cdot kg^{-1} \cdot K^{-1}$, respectively. The measured scattering function $S(Q,E)$s (**Fig. 3a, 3b**) exhibit pronounced QENS signal for n-hexane and ethyl acetate, whereas 1,3-butanediol shows a much narrower broadening, indicating strongly hindered dynamics within the instrument time window. QENS spectra are well described by a two-Lorentzian function model[26] (**Extended Data Fig. 5**). Details of the analysis procedure and more QENS spectra are provided in Methods.

The Q-dependence of the extracted linewidths reflects the characteristics of the relaxation processes. For n-hexane and ethyl acetate, the half-width at half-maximum (HWHM) of the narrow Lorentzian component, Γ_n, increases approximately linearly

with Q^2 in the low-Q region (**Fig. 3c**), a hallmark of long-range translational diffusion governed by Fick's second law[26]. In contrast, Γ_n for 1,3-butanediol is close to the instrumental resolution and shows only weak Q-dependence (**Fig. 3c**). The extracted diffusion coefficient of 1,3-butanediol (~1×10^{-10} $m^{-2}\cdot s^{-1}$) is one order of magnitude lower than that of n-hexane (~4×10^{-9} $m^{-2}\cdot s^{-1}$) and ethyl acetate (~3×10^{-9} $m^{-2}\cdot s^{-1}$). Such long-range diffusion is significantly suppressed under pressure, leading to a markedly reduced diffusion coefficient (see the case of ethyl acetate as an example, **Extended Data Fig. 6**). The HWHM of the broad Lorentzian component (Γ_b) shows little dependence on Q^2 for the three liquids, indicating localized and faster molecular motions[27](**Fig. 3d**).

The elastic incoherent structure factor (EISF) provides further insight into the geometry of molecular fast motions. EISFs for n-hexane and Ethyl acetate are well described by the isotropic rotation model (**Fig. 3e**)[28], with a rotation radius of ~1.6 Å and ~1.3 Å, respectively. The rotation radii basically match the distance of the hydrogen atoms from the carbon chain, indicating rapid rotation of the whole molecule about its long axis[26, 28]. By contrast, the EISF for 1,3-butanediol is better captured by the two-site jump model[28] (**Fig. 3e**), where the fast motion corresponds to local conformational variations involving specific hydrogen atoms, e.g., jumps between different sites of -OH or -CH_2 groups[29]. The displacement of the hydrogen atom between the two sites is about 1 Å. Detailed fitting profiles for all the possible models are plotted in **Extended Data Fig. 7.**

The above QENS results provide a microscopic basis for the observed variation in $|\Delta S|$ among the three liquids: the more restricted the molecular motion under ambient conditions, the smaller the entropy reduction under pressure. In the following section, we further elucidate the diversity of liquid-state BC effects by correlating them with molecular structural features.

Mechanistic diversity of liquid-state barocaloric effects

To uncover how different molecular degrees of freedom contribute to the BC effects, we performed molecular dynamics (MD) simulations on the three liquids whose molecular structures are shown in **Fig. 4a**. The MD results show that n-hexane exhibits the largest total entropy, while 1,3-butanediol shows the smallest value (**Fig. 4b**), which accords well with the differently constrained molecular motions revealed by QENS (**Fig.**

3). As pressure increases, the total entropy decreases gradually, and this trend is more pronounced for n-hexane and ethyl acetate than for 1,3-butanediol. Decomposing the entropy into rotational (Rot), translational (Tra), and vibrational (Vib) contributions[25], we find that the Rot and Tra parts are far more pressure-dependent than the Vib part (Fig. 4c). Rot and Tra contributions account for more than 80 % of the total $|\Delta S|$ at 100 MPa, rising to 90 % at 300 MPa. This unambiguously identifies the pressure-induced suppression of molecular motions as the origin of the colossal BC response.

The binding-energy curves were calculated using density functional theory (DFT) in order to understand liquid-state BC behavior from the energetic landscapes. As shown in Fig. 4d, 1,3-butanediol has a much deeper well (-0.95 eV) than ethyl acetate and n-hexane (~ -0.65 eV), with curvature following the order 1,3-butanediol > ethyl acetate > n-hexane. Curvature directly governs the elastic stiffness of the intermolecular interaction: a larger curvature corresponds to a higher bulk modulus and, consequently, lower compressibility. These differences arise from the molecular structures (Fig. 4a). The weakly polar C-H dipoles in n-hexane cancel tetrahedrally, making the molecule nonpolar and leaving only soft dispersion forces[30], which yield the flattest potential. In contrast, 1,3-butanediol bears two fully exposed hydroxyl groups, giving a larger dipole (~2.5 D[31]) and, more importantly, a robust HB network through donor-acceptor synergy[30, 32]. The highly directional and electrostatic nature of the HB network produces the steepest repulsive wall upon compression[33], and strongly restricts molecular dynamics (Fig. 3). Ethyl acetate contains a polar ester group (C=O) with a dipole moment of ~1.8 D[31], but lacks O–H groups and therefore cannot form HB, resulting in moderate stiffness. We note that dispersion forces strengthen with increasing molecular size. That is why we selected the three liquids with nearly the same molecular weight to study how structural features determine intermolecular interactions and the BC effect.

MD simulations of the radial distribution function $g(r)$ reveal that at 200 MPa, n-hexane exhibits the largest shift in $g(r)$ (Fig. 4e). The coordination number within 20 Å increases by 12.3%, higher than ethyl acetate (9.1%) and 1,3-butanediol (5.1%) (inset of Fig. 4e), which is opposite to the order of binding energy curvatures (Fig. 4d). Strikingly, 1,3-butanediol shows a prominent second-nearest-neighbor $g(r)$ peak at ~10Å, indicating a high degree of local order imposed associated with the HB network. Under pressure, the first $g(r)$ peak of 1,3-butanediol increases in height while the first

valley deepens, reflecting enhanced local order[23], yet the intermolecular distances change little.

Integrating the DFT energy landscapes with $g(r)$ evolutions, the distinct BC mechanisms of the three liquids now emerge clearly. For n-hexane, the soft, flat potential means that applying pressure reduces intermolecular distances, exactly as seen in the large g(r) shift. Such a physical compaction strongly suppresses rotational and translational degrees of freedom, yielding a large entropy change, but at the cost of a substantial volume reduction (**Extended Data Fig. 8**). For 1,3-butanediol, however, the strong confinement imposed by the steep potential well makes shrinking the intermolecular spacing energetically unfavorable. Instead, the mechanical work drives a cooperative, directional reorientation of the molecules, which directly enhances local structural order. This pathway results in a more moderate entropy change but with a much smaller volume penalty. Ethyl acetate, possessing polar interactions but lacking a HB network, falls in between. In most molecular liquids, especially mixtures, multiple types of intermolecular interactions coexist, and the above BC mechanisms are expected to superimpose. The framework reveals here therefore guides the assessment and design of liquid-state BC materials based on their intermolecular interaction profiles.

Conclusion

In summary, we establish liquid-state BC refrigeration, characterized by its inherent reversibility, as a fundamentally new class of cooling technology distinct from conventional VCR and emerging SSC approaches. Without invoking a liquid-solid phase transition, several molecular liquids exhibit colossal thermal responses with $|\Delta T_{ad}|$ of 30 K and $|\Delta S|$ of 230 $J{\cdot}kg^{-1}{\cdot}K^{-1}$, arising from pressure-confined translational and rotational molecular motions, as revealed by MD and QENS. This continuous entropy reduction affords an exceptionally wide operating temperature window of up to 150 K, yielding a RCP of approximately 10^4 $J{\cdot}kg^{-1}$, at least two times that of state-of-the-art SSC materials. In a Carnot-like cycle, the liquid-state BC system achieves a COP of 37.5 over an 8 K temperature span and delivers a cooling capacity of 80 $J{\cdot}g^{-1}$. More broadly, the concept extends naturally to other liquid classes, including, but not limited to ionic liquids and liquid metals, offering a versatile platform for next-generation sustainable cooling technologies.

Online content

Any methods, additional references, Nature Portfolio reporting summaries, source data, extended data, supplementary information, acknowledgments, peer review information, details of author contributions and competing interests, and statements of data and code availability are available at

References

1. Perkins Vapor-Compression Cycle for Refrigeration: A Historical Mechanical Engineering Landmark. *ASME* (2020).
2. The Importance of Energy Efficiency in the Refrigeration, Air-conditioning and Heat Pump Sectors (United Nations Environmental Programme, 2018).
3. 22nd Conference of the Parties (CoP22) to the United Nations Framework Convention on Climate Change (UNFCCC) (Marrakech, Morocco; 2016).
4. Sun, Y. et al. Materials with the barocaloric effect for solid-state refrigeration. *J. Mater. Chem. A* **13**, 6152-6175 (2025).
5. Zhang, K. et al. Colossal Barocaloric Materials. *Ann. Rev. Mater. Res.* **56**, 109-134 (2026).
6. Moya, X. & Mathur, N.D. Caloric materials for cooling and heating. *Science* **370**, 797-803 (2020).
7. Zhang, K. et al. Extreme barocaloric effect at dissolution. *Nature* **649**, 1180-1185 (2026).
8. Lilley, D. & Prasher, R. Ionocaloric refrigeration cycle. *Science* **378**, 1344-1348 (2022).
9. Kim, S. et al. Liquid-state dipolarcaloric refrigeration cycle with nitrate-based salts. *Science* **390**, eadz7967 (2025).
10. Shen, B. G., Sun, J. R., Hu, F. X., Zhang, H. W. & Cheng, Z. H. Recent Progress in Exploring Magnetocaloric Materials. *Adv. Mater.* **21**, 4545-4564 (2009).
11. Zheng, S. et al. Colossal electrocaloric effect in an interface-augmented ferroelectric polymer. *Science* **382**, 1020-1026 (2023).
12. Ma, R. et al. Highly efficient electrocaloric cooling with electrostatic actuation. *Science* **357**, 1130-1134 (2017).
13. Qian, S. et al. High-performance multimode elastocaloric cooling system. *Science* **380**, 722-727 (2023).
14. Li, B. et al. Colossal barocaloric effects in plastic crystals. *Nature* **567**, 506-510 (2019).
15. Piper, S. L. et al. Organic ionic plastic crystals having colossal barocaloric effects for sustainable refrigeration. *Science* **387**, 56-62 (2025).
16. Aznar, A. et al. Reversible colossal barocaloric effects near room temperature in 1-X-adamantane (X=Cl, Br) plastic crystals. *Appl. Mater. Today* **23**, 101023 (2021).
17. Li, J. N. et al. Colossal Reversible Barocaloric Effects in Layered Hybrid Perovskite $(C_{10}H_{21}NH_3)_2MnCl_4$ under Low Pressure Near Room Temperature. *Adv. Funct. Mater.* **31**, 2105154 (2021).

18. Gao, Y. H. et al. Low pressure reversibly driving colossal barocaloric effect in two-dimensional vdW alkylammonium halides. *Nat. Commun.* **15**, 1838 (2024).
19. Romanini, M. et al. Giant and Reversible Barocaloric Effect in Trinuclear Spin-Crossover Complex $Fe_3(bntrz)_6(tcnset)_6$. *Adv. Mater.* **33**, e2008076 (2021).
20. Ohkoshi, S. I. et al. Giant adiabatic temperature change and its direct measurement of a barocaloric effect in a charge-transfer solid. *Nat. Commun.* **14**, 8466 (2023).
21. Dai, Z. et al. Thermodynamic Analysis on the Performance of Barocaloric Refrigeration Systems Using Neopentyl Glycol as the Refrigerant. *J. Therm. Sci.* **32**, 1063-1073 (2023).
22. Masche, M., Ianniciello, L., Tušek, J. & Engelbrecht, K. Impact of hysteresis on caloric cooling performance. *Int. J. Refrig.* **121**, 302-312 (2021).
23. Lin, J. et al. Colossal and reversible barocaloric effect in liquid-solid-transition materials n-alkanes. *Nat. Commun.* **13**, 596 (2022).
24. Watson, K. M. Thermodynamics of the Liquid State. *Ind. Eng. Chem.* **35**, 398-406 (1943).
25. Pascal, T. A., Lin, S. T. & Goddard, W. A., 3rd Thermodynamics of liquids: standard molar entropies and heat capacities of common solvents from 2PT molecular dynamics. *Phys. Chem. Chem. Phys.* **13**, 169-181 (2011).
26. Hofmann, T. et al. Molecular dynamics of n-hexane: a quasi-elastic neutron scattering study on the bulk and spatially nanochannel-confined liquid. *J. Chem. Phys.* **136**, 124505 (2012).
27. Kyriakos, K. et al. Solvent Dynamics in Solutions of PNIPAM in Water/Methanol Mixtures—A Quasi-Elastic Neutron Scattering Study. *J. Phys. Chem. B.* **120**, 4679-4688 (2016).
28. Fernandez-Alonso, F., Price, D. L. Neutron Scattering - Applications in Biology, Chemistry, and Materials Science 349-401 (2017).
29. Abdel-Rahman, M. A., Morse, M. K. & Zhao, H. Theoretical prediction of the dehydration mechanism of 1, 3-butanediol as a potential biofuel surrogate. *Theor. Chem. Acc.* **144**, 1 (2024).
30. Zeegers-Huyskens, T. & Huyskens, P. in Intermolecular Forces: An Introduction to Modern Methods and Results. (eds. P.L. Huyskens, W. A. P. Luck & T. Zeegers-Huyskens) 1-30 (Springer Berlin Heidelberg, Berlin, Heidelberg; 1991).
31. Yaws, C.L. & Narasimhan, P.K. in Thermophysical Properties of Chemicals and Hydrocarbons. (ed. C.L. Yaws) 672-682 (William Andrew Publishing, Norwich, NY; 2009).
32. Eterno Fileti, E., Voroshylova, I. V., Ferreira, E. S. C., Natália D. S. Cordeiro, M. & Malaspina, T. Ab initio molecular dynamics study of hydroxyl positioning in butanediol and its impact on deep eutectic solvent structure. *J. Mol. Liq.* **409**, 125548 (2024).
33. Metcalf, D. P., Smith, A., Glick, Z. L. & Sherrill, C. D. Range-dependence of two-body intermolecular interactions and their energy components in molecular crystals. *J. Chem. Phys.* **157**, 084503 (2022).

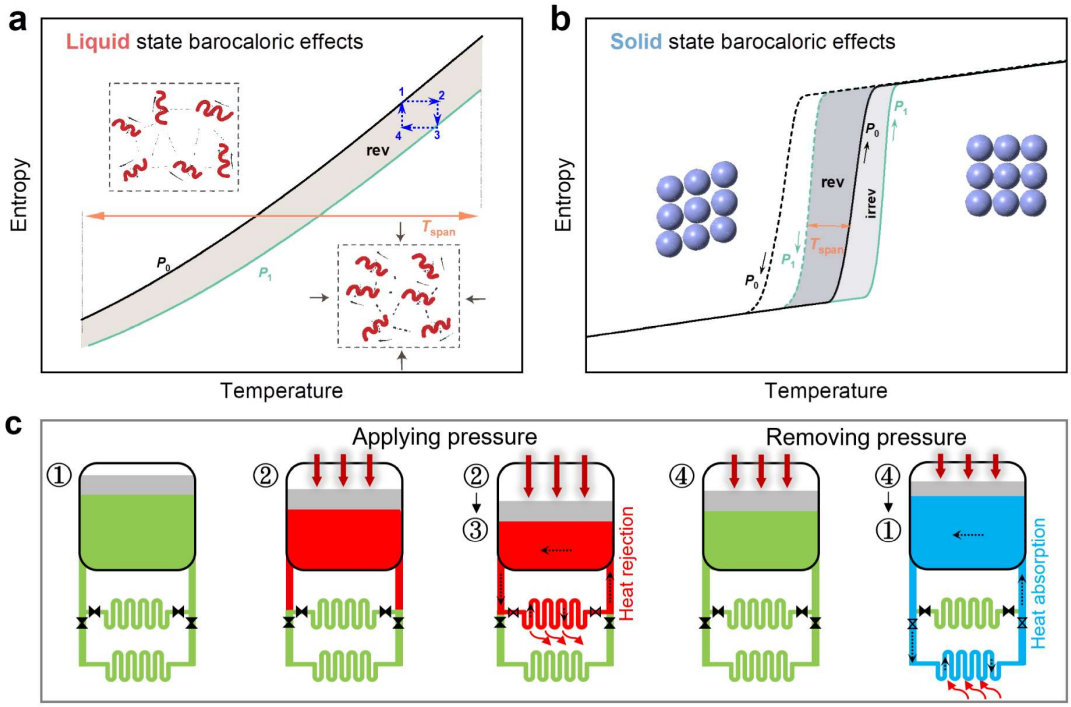


Fig. 1 | Liquid-state BC refrigeration. a, b, Comparison of entropy-change mechanisms between liquid-state (**a**) and solid-state (**b**) BC effects, highlighting the broader temperature span (T_{span}) and absence of thermal hysteresis in liquids. **c,** Schematic of a Carnot-like refrigeration cycle based on the liquid-state BC effect, comprising four reversible steps: ① initial stage at ambient pressure; ② isentropic compression, raising the liquid temperature; ②→③ isothermal heat release to the surroundings upon further compression; ④ isentropic depressurization, leading to a temperature decrease of the liquid; ④→① isothermal heat absorption from the cold reservoir with further release of pressure. During steps ②→③ and ④→①, the refrigerant flow (indicated by arrows) is driven by a pump. The four steps are also shown in **a**.

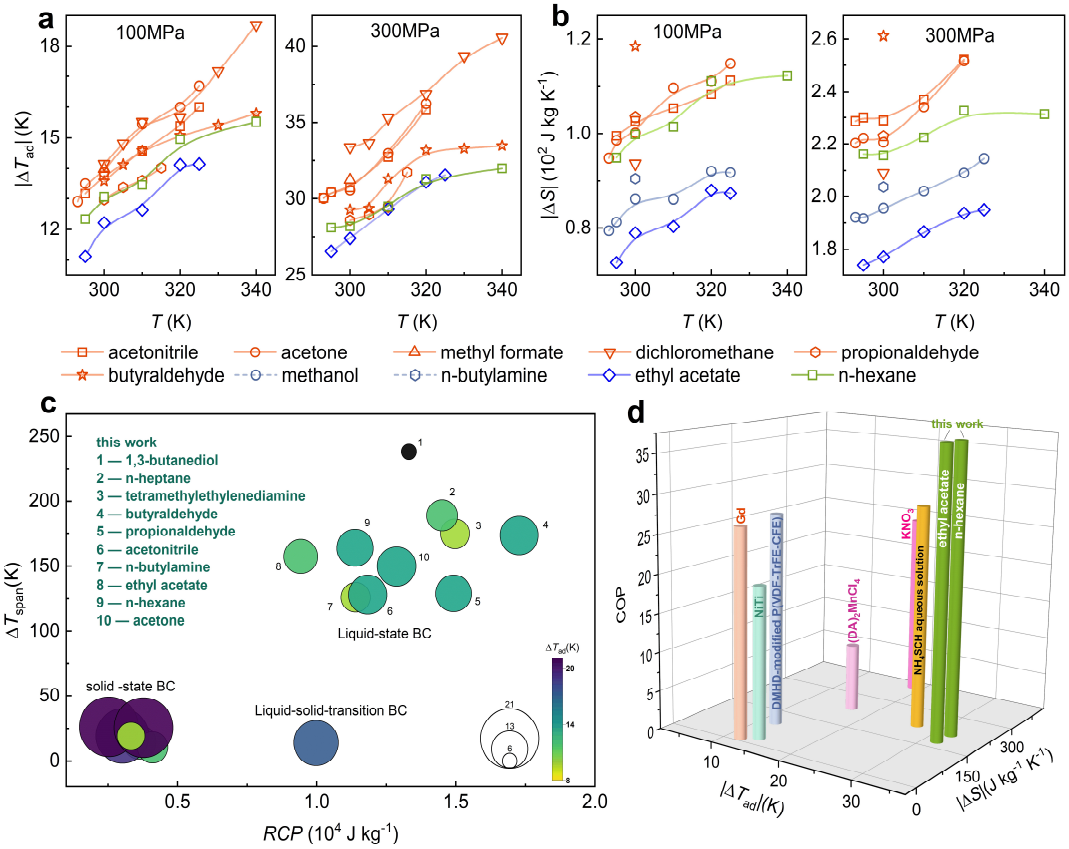


Fig. 2 | Liquid-state BC effects and the refrigeration performance of molecular liquids. a, Adiabatic temperature change ($|\Delta T_{ad}|$) measured at 100 MPa and 300 MPa for selected liquids. **b**, Entropy change ($|\Delta S|$) derived from $|\Delta T_{ad}|$ in **a**. **c**, Comparison of working temperature range (T_{span}) and Relative Cooling Power (RCP) of the selected liquids and representative BC materials with first-order phase transition. **d**, The COP, reversible $|\Delta T_{ad}|$ and $|\Delta S|$ of liquid-state BC, typical SSC, and liquid-state dipolar-caloric and resolution-BC materials.

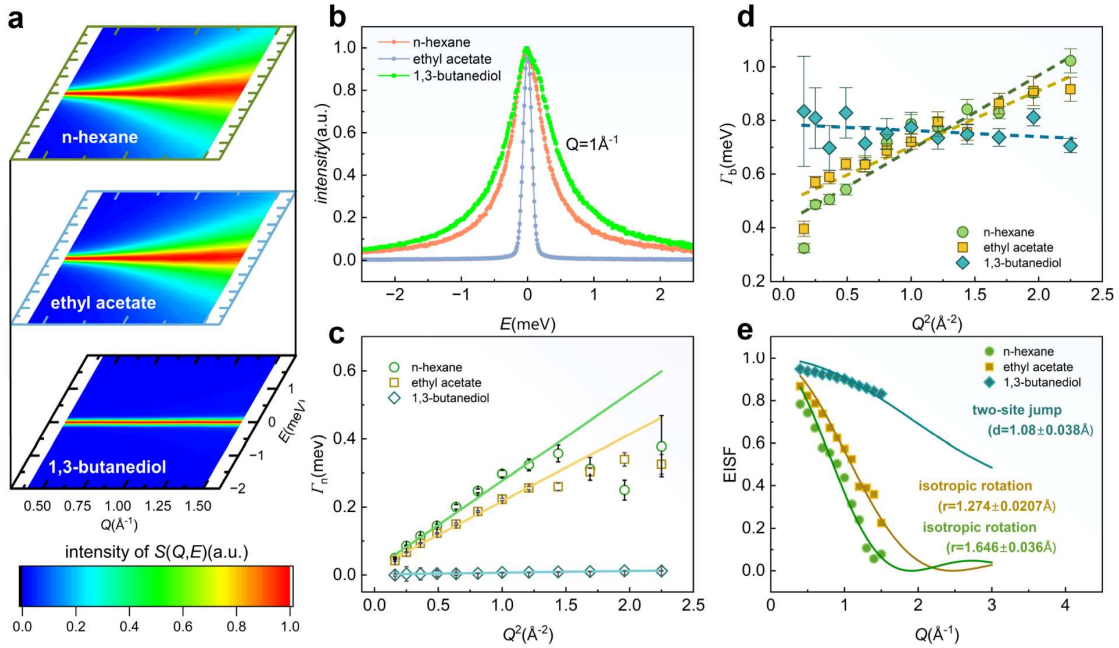
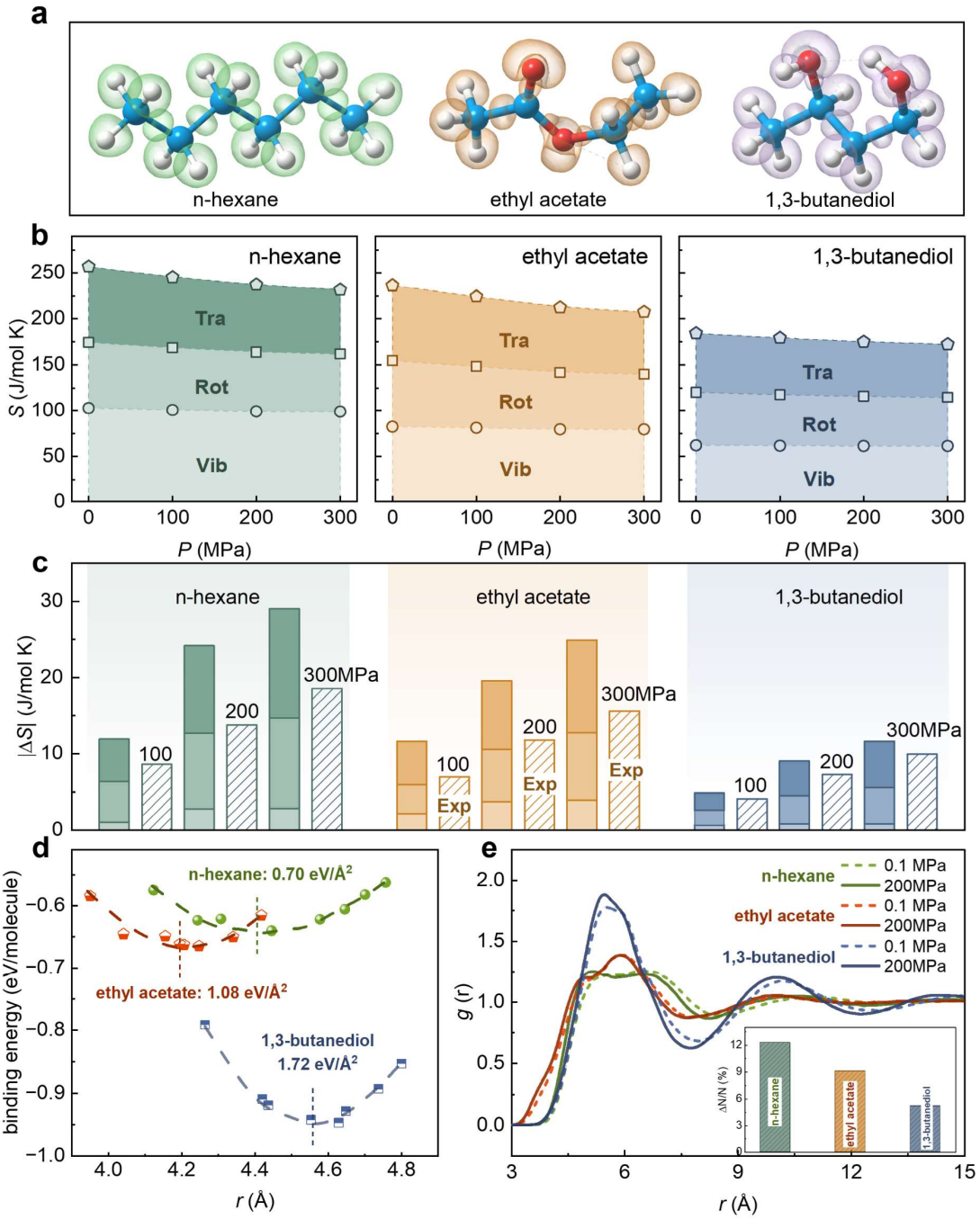


Fig. 3 | Dynamics of typical liquids from Quasi-elastic neutron scattering (QENS) spectra. **a**, QENS spectra for n-hexane, ethyl acetate, and 1,3-butanediol. **b**, Comparison of S(Q, E)s at Q = 1 Å for the three liquids. **c**, Q^2 dependence of the HWHM associated with long-range slow diffusions, Γ_n. Linear fits (solid lines) were used to extract the diffusion coefficient. **d**, Q^2-dependence of the HWHM corresponding to local fast motions, Γ_b. Dotted lines are for guidance. **e**, Elastic incoherent structure factor (EISF) fitted with the isotropic rotation model for n-hexane and ethyl acetate, and with the two-site jump model for 1,3-butanediol. The rotation radii (r) for the rotation model and the displacement magnitude (d) of the hydrogen atom in the two-site jump model are marked.



375

376 **Fig. 4 | Energetic landscape, local structures, and the diversity of liquid-state BC**
377 **effects**. **a**, Molecular structures of n-hexane, ethyl acetate, and 1,3-butanediol with
378 electron localization function (ELF, isosurface=0.8). **b**, MD-simulated total molar
379 entropy with rotational (Rot), translational (Tra), and vibrational (Vib) contributions
380 under various pressures. **c**, The MD-calculated total molar $|\Delta S|$ under pressure and its
381 decompositions, along with the experimental ones. **d**, Intermolecular binding energy as
382 a function of molecular center-of-mass separation (r), calculated from DFT. **e**, Radial

distribution function g(r) at 0.1 MPa and 200 MPa calculated by MD. The change of coordination number (N) within 20 Å at 200 MPa is shown in the inset.

Methods

Adiabatic temperature change measurement. 23 liquids with at least 2N purity including n-hexane, n-heptane, n-octane, acetonitrile, acetone, 3-pentanone, methyl formate, ethyl acetate, ethyl propionate, dimethyl carbonate, dichloromethane, propionaldehyde, butyraldehyde, tetramethylethylenediamine, dimethylformamide, methanol, ethanol, 1-propanol, 1-butanol, 1,3-butanediol, 1-hexanol, n-butylamine, butyric acid were purchased from either Aladdin (Shanghai China), or Sinopharm Reagent (Shanghai China), or Macklin (Shanghai China). The direct measurements of the adiabatic temperature change (ΔT_{ad}) were carried out on our home-built High-Pressure Differential Analysis (HP-DTA) system[23, 34]. Due to the high liquidity of liquids and extremely low modulus, the liquids themselves served as the pressure medium. The test temperature varies from 295 K to 360 K. The data were collected in both the pressure loading and unloading processes. Details of measuring ΔT_{ad} can be found in ref[23]. The ΔT_{ad} of ethyl acetate was measured with pressure cycling between 0.1 and 100 MPa for 20 cycles at 20 MPa/s.

Deduction of isothermal entropy change from the adiabatic temperature change. The ΔS driven by pressure can be calculated by $\Delta S(\mathrm{P})=\Delta T_{ad} C_p(\mathrm{P})/T_0$[35], where C_p(P) is the specific heat under pressure at the test temperature (T_0). As C_p(P) is unavailable for many liquids, we used C_p at ambient pressure instead (Supplementary Table S1). This assumption may lead to an overestimation of ΔS by 2-8% (Supplementary Fig. S23). However, the setup for measuring ΔT_{ad} was not exactly adiabatic. Therefore, the observed ΔT_{ad} value is lower than the true one, which underestimates the ΔS and partially offsets the aforementioned overestimation.

Evaluation of refrigeration performance. In a Carnot-like thermodynamic cycle, the coefficient of performance (COP) for cycle refrigeration can be calculated as $COP=\frac{Q_L}{Q_H-Q_L}$, where Q_L and Q_H are the heat exchanged in the two isobaric processes with the cold reservoir and heat sink, respectively[21]. The heat absorbed from cold reservoir in each refrigeration cycle is given by[21] $Q_L=\int_{s_4}^{s_1} T\mathrm{d}s$ (**Extended Data Fig. 3**).

Quasi-elastic neutron scattering. Quasi-elastic neutron scatterings (QENS) were performed using the cold-neutron time-of-flight spectrometer Pelican, at Australian Nuclear Science and Technology Organisation (ANSTO). The instrument was configured with an incident neutron wavelength of 4.69 Å, affording a neutron energy of 3.7 meV with an energy resolution of 0.13 meV at the elastic peak[36]. For ambient-pressure measurement, liquids (n-hexane, ethyl acetate, and 1,3-butanediol) were loaded in an annular aluminum can with a gap thickness of 0.1 mm. An identical empty cell was also measured for background subtraction. A standard vanadium cylinder was measured for detector normalization. QENS at 500 MPa of ethyl acetate was also measured using a hybrid CuBe/NiCrAl cell[37]. The data reduction, including background subtraction and detector normalization, and data analysis were performed using the Large Array Manipulation Program (LAMP) software[38]. The $S(Q, E)$ data were fitted to Eq. (1) using the QENS_FIT module embedded in LAMP. The data were fitted with two Lorentzian functions, plus a delta function and a linear background, convoluted with the instrumental resolution function determined by vanadium.

Let us consider the total incoherent scattering cross section results from the independent superposition of a long-range diffusional process characterized by a Lorentzian function with a narrow HWHM (Γ_n) and a localized motion represented by a Lorentzian function having a wider HWHM (Γ_b) [26]. The total scattering function is given by:

$$S_{ic}^{total}(Q,\omega)=S_{ic}^{trans}(Q,\omega)+S_{ic}^{loc}(Q,\omega) \quad (1)$$

$$S_{ic}^{trans}(Q,\omega)=\frac{1}{\pi}\frac{\Gamma_n}{\hbar^2\omega^2+\Gamma_n} \quad (2)$$

$$S_{ic}^{loc}(Q,\omega)=EISF(Q)\delta(\omega)-\frac{1-EISF(Q)}{\pi}*\frac{\Gamma_b}{\hbar^2\omega^2+\Gamma_b^2} \quad (3)$$

The elastic incoherent structure factor (EISF) is defined as the ratio of the elastic intensity to the total intensity, which reflects the spatial constraints imposed on local random motions. Because there are two Lorentzian functions at 300 K, the EISF is defined as[14]

$$EISF_{\text{trans}}=\frac{I_{\text{elastic}}}{I_{\text{elastic}}+I_{\text{QENS,narrow}}}\ , \tag{4}$$

$$EISF_{\text{loc}}=\frac{I_{\text{elastic}}+I_{\text{QENS,narrow}}}{I_{\text{elastic}}+I_{\text{QENS,narrow}}+I_{\text{QENS,broad}}}\ , \tag{5}$$

Here, I_{elastic}, $I_{\text{QENS,narrow}}$ and $I_{\text{QENS,broad}}$ are the intensities of the elastic signal (Delta function), narrow Lorentzian function, and broad Lorentzian function, respectively.

The EISF of the fast mode (i.e., the local motion) for ethyl acetate and n-hexane can be fitted using the isotropic rotation model, with the EISF given as[28] $EISF=\left[\frac{\sin(QR)}{QR}\right]^2$, where R is the radius of rotation (the distance from the hydrogen atom to the center of rotation). For 1,3-butanediol, the two-site jump model[28] gives a better fit, where $EISF=\frac{1}{2}[1+\frac{\sin(Qd)}{Qd}]$, and d is the magnitude of the displacement of the hydrogen atom between the two sites.

Theoretical calculation methods. Classic molecular dynamics (MD) simulations are performed using the LAMMPS package[39]. The all-atom Optimized Potentials for Liquid Simulations (OPLS-AA) force field[40] is used to describe the interatomic potentials of the liquid molecules. The bond, angle, dihedral, and Lennard-Jones OPLS-AA parameters are provided using LigParGen[41-43]. The molecular liquid system is modeled by randomly putting 500 molecules in a simulation box based on the liquid density using the fftool[44] and packmol[45] packages. To simulate the thermal properties of molecular liquid, the NVT ensemble is firstly used to equilibrate the system for 10 ps at 300 K. Then, the NPT ensemble is carried out for 0.2 ns to simulate the effect of isotropic pressure (at the ambient condition, 100, 200 and 300 MPa) at 300 K. After that, 20 ps NVT-MD is performed at 300 K, and each MD step collects the energies, atomic positions, velocities etc. Based on these data, we can calculate the entropies (including translation, rotation, and vibration contributions) using the two-phase thermodynamics (2PT) program[25].

The Density-functional theory (DFT) calculations were carried out by choosing a small system with 20-30 molecules using the Fritz Haber Institute ab initio materials simulations (FHI-aims) with the all-electron numeric atomic-centered basis functions[45]. We used the light basis sets with the 2020 species defaults for C, O, and H. We used the generalized gradient approximation of Perdew, Burke, and Ernzerhof (GGA-PBE)[46] for the electronic exchange-correlation functional. We used the Tkatchenko-Scheffler method to enable the nonlocal van der Waals correction[47]. To simulate the behavior of disordered molecules, we used a large unit cell (> 16 Å), and a Γ point was sufficient to sample the Brillouin zone. Atomic positions are relaxed until all the forces are below 0.01 eV/Å.

Data availability

All relevant data that support the findings of this study are presented in the manuscript and supplementary information file. Source data are available from the corresponding author upon reasonable request.

Acknowledgments

This work was supported by the National Natural Foundation of China (No.12474025) and the HFIPS Director's Fund (No. BJPY2023A08). Y. Z. acknowledges financial support from the National Natural Science Foundation of China (No. 12474016) and the program of "Distinguished Expert of Taishan Scholar" (No. tstp20221124). Access to the Pelican instrument at ANSTO through proposal P18704 is gratefully acknowledged.

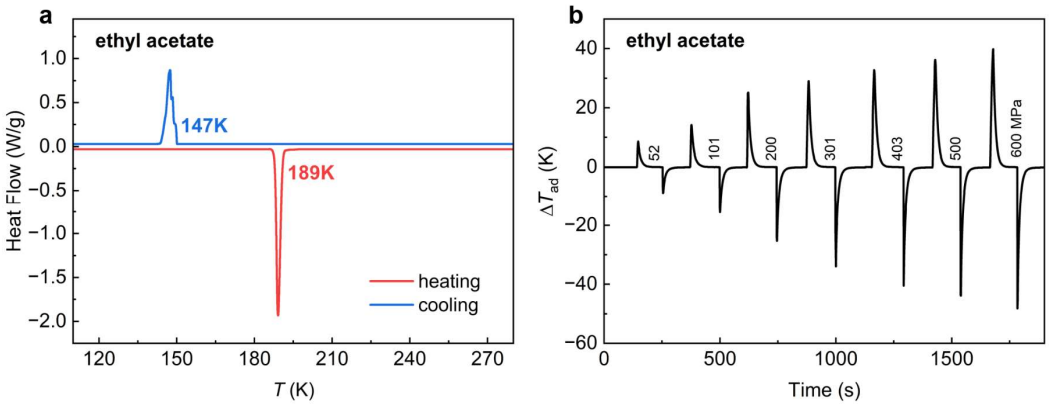
Author contributions

P. T., J. L. and Y. S. conceived the study. P. T., Y. Z., D. Y. and B. L. planned the research. T. X., R. J., Z. L. and W. S. performed the adiabatic temperatures and processed the data analysis. Y. Z. and X. L. performed the MD and DFT calculations and analysis. D. Y. and B. Y. carried out the QENS. K. L. and D. Y. processed and analyzed the QENS data. K. Z. and Y. L. designed and

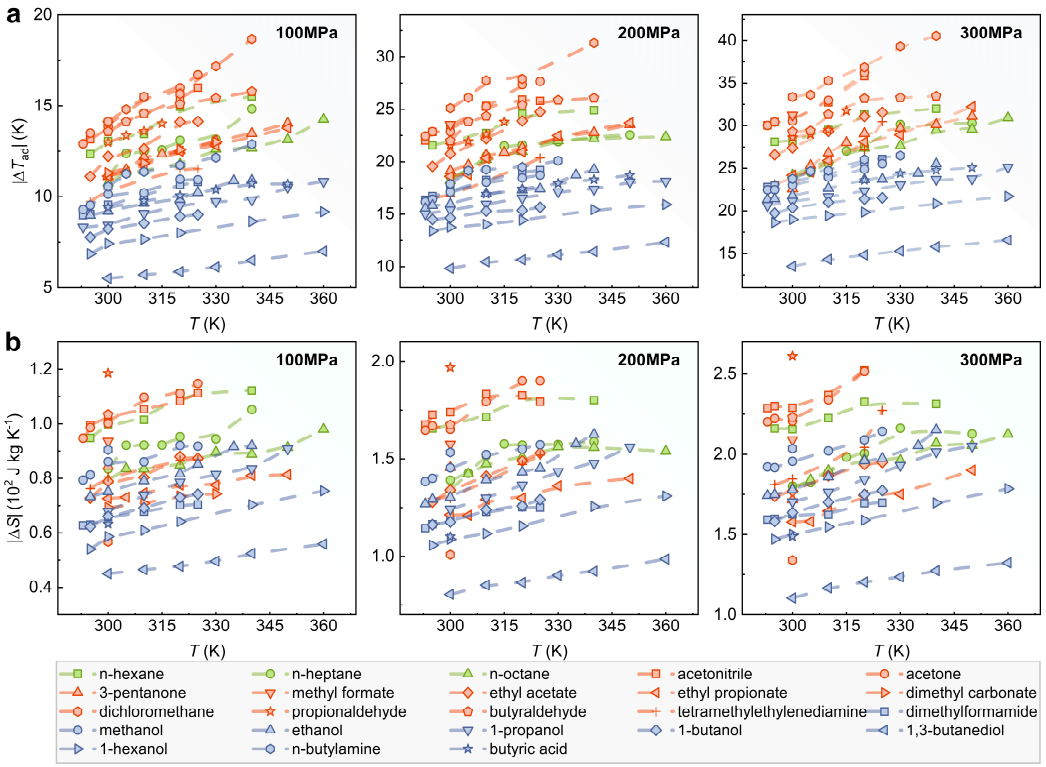
performed the material durability test. T. X. and K. L. prepared all the figures and tables. J. L. and P. T. wrote the manuscript with discussion and input from all coauthors.

Competing interests

The authors declare no competing interests.



Extended Data Fig. 1 | Melting and solidification of ethyl acetate. a, The DSC scanning of the melting and solidification. **b**, The temperature change under pressure loading and releasing up to 600 MPa.

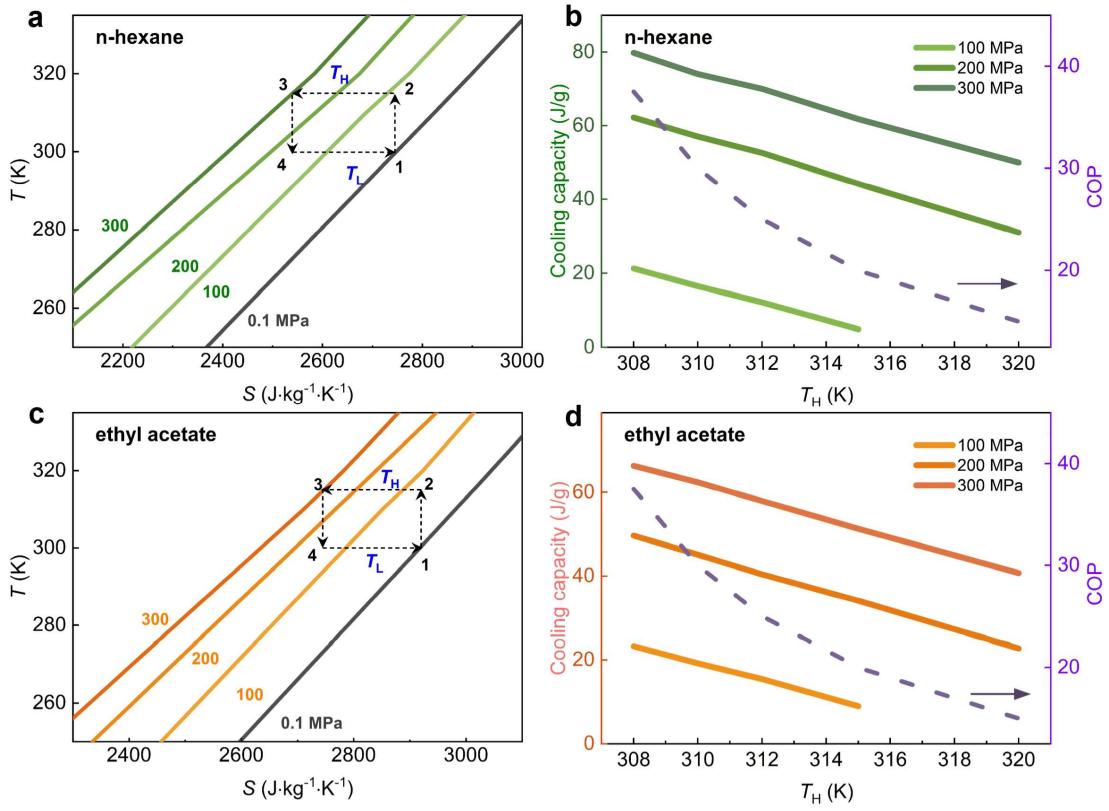


488

489 **Extended Data Fig. 2 | The $|\Delta T_{ad}|$ and $|\Delta S|$ for 23 molecular liquids at 100, 200 and**

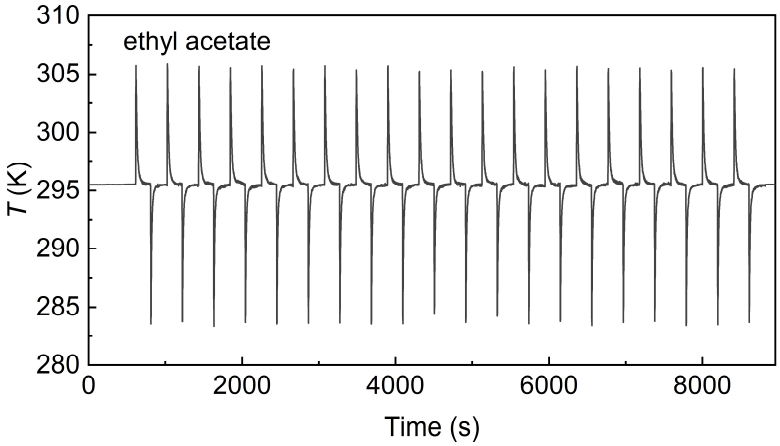
490 **300 MPa.**

491

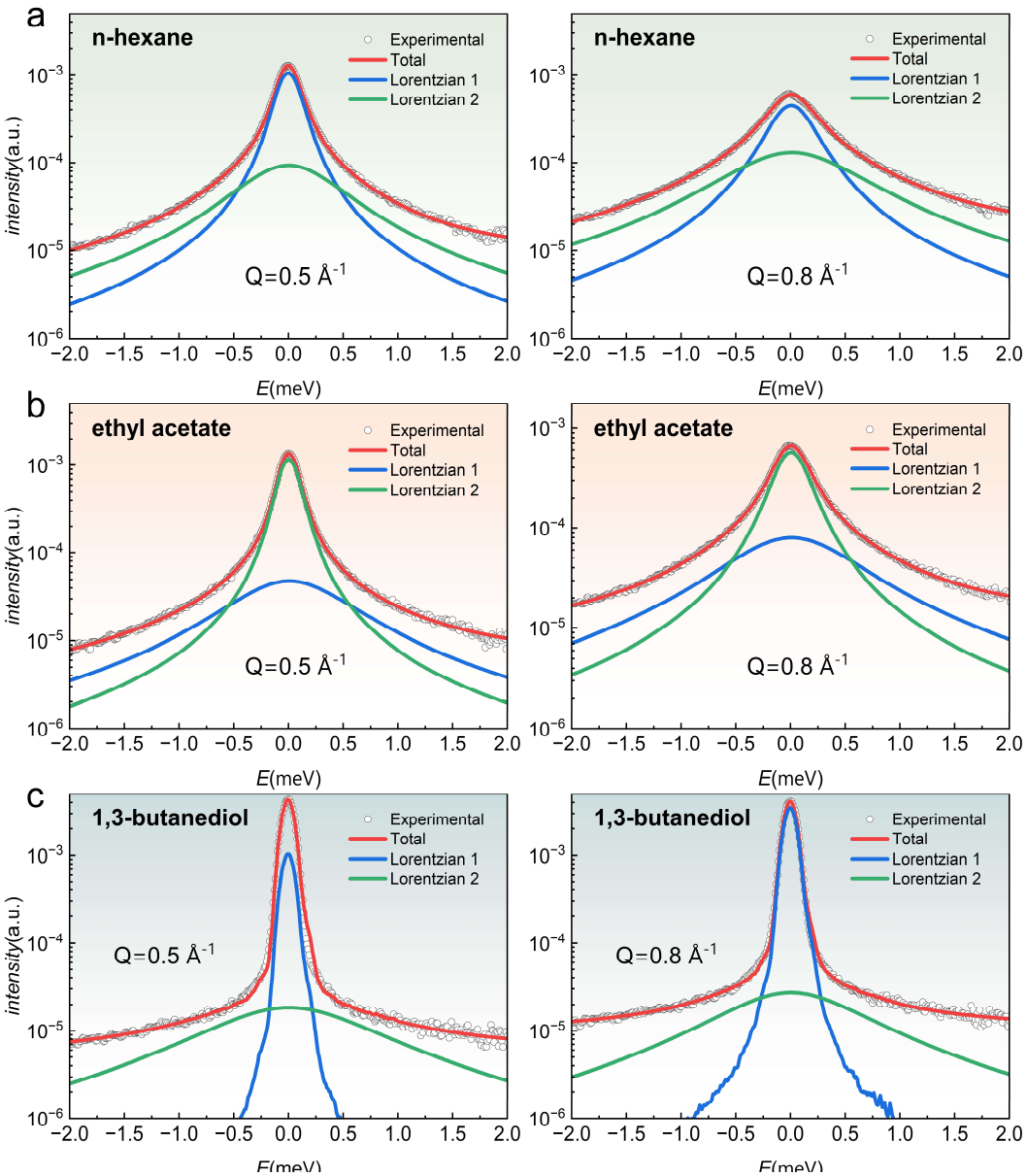


492

Extended Data Fig. 3 | The performance of Carnot-like refrigeration based on the liquid-state barocaloric effect. a, The MD-calculated temperature-entropy plots, and **b,** the coefficient of performance (COP) and cooling capacity as a function of the heat sink temperature (T_H) for n-hexane. **c**, The MD-calculated temperature-entropy plots, and **d**, COP and cooling capacity as a function of T_H for ethyl acetate. The refrigeration cycle follows the sequence 1→2→3→4. T_L (set as 300 K) is the temperature of the cold reservoir.



Extended Data Fig. 4 | The durability of the liquid-state Barocaloric effect. The temperature variation of ethyl acetate with loading and unloading pressure of 100 MPa (± 5 MPa) for twenty cycles.



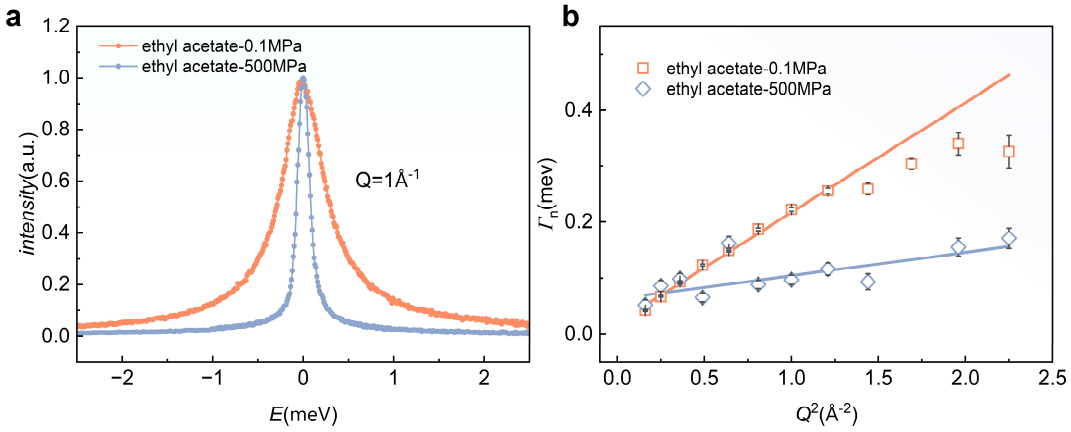
506

507 **Extended Data Fig. 5 | Representative *S*(Q, E) spectra with different *Q* ranges are**

508 **fitted by a two-Lorentzian function. a**, for n-hexane, **b**, for ethyl acetate, and **c**, for

509 1,3-butanediol.

510



511

512 **Extended Data Fig. 6 | Comparison of the Quasi-elastic neutron scattering (QENS)**

513 **spectra at 0.1 MPa and 500 MPa. a**, A comparison of the $S(Q, E)$s with Q=1Å for

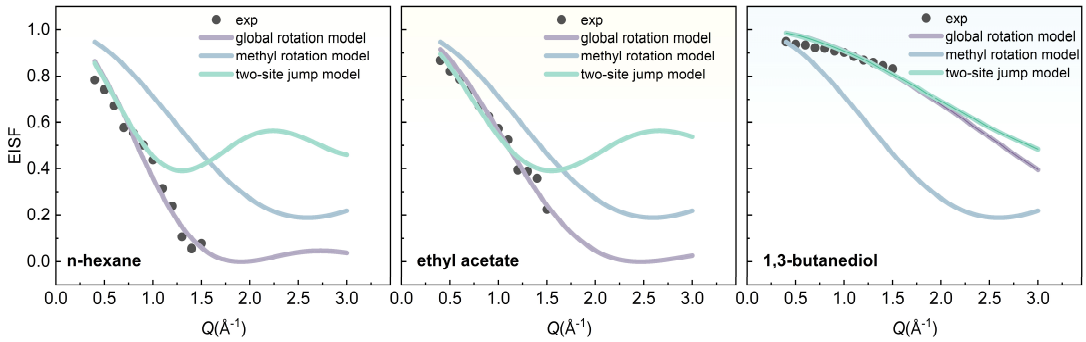
514 ethyl acetate at 0.1 MPa and 500 MPa. **b**, The Q^2-dependence of the linewidths (Γ_n) of

515 long-range slow diffusions at 0.1 MPa and 500 MPa. Linear fitting (solid lines) was

516 used to obtain the diffusion coefficient.

517

518



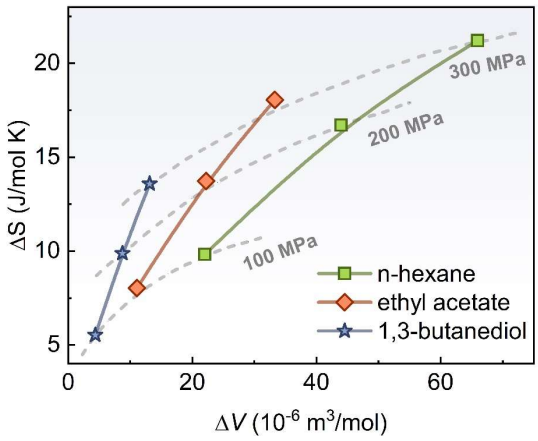
519

520 **Extended Data Fig. 7 | A comparison of fits to the elastic incoherent structure**

521 **factor (EISF) with different models for n-hexane, ethyl acetate, and 1,3-butanediol.**

522

523



Extended Data Fig. 8 | MD-calculated molar entropy change (Δ*S*) as a function of molar volume change (Δ*V*) at different pressures for n-hexane, ethyl acetate, and 1,3-butanediol.

Extended Data Table 1 | Data used in Fig. 2c. All the data listed are at 100 MPa.

Material	ΔT_{ad} (K)	ΔS_{rev} ($J \cdot kg^{-1} \cdot K^{-1}$)	temperature range (K)	RCP ($J \cdot kg^{-1}$)	ref
$(C_{10}H_{21}NH_3)_2MnCl_4$	12	250	14.5	3625	17
1-Cl-ada	19	159	19	3021	16
$(CH_3\text{-}(CH_2)_9)_2NH_2Cl$	11	390	10.5	4103	18
$Fe_3(bntrz)_6(tcnset)_6$	21	97	26	2533	19
cyano-RbMnFeCo	21	148	25.5	3779	20
$LiCB_{11}H_{12}$	10	200	19	3325	48
$C_{16}H_{34}$	16	739	14	9979	23
n-hexane	13.06	69.38	164	11379	This work
n-heptane	11.13	76.75	189	14508	This work
ethyl acetate	12.22	59.84	157	9425	This work
acetonitrile	13.77	92.46	128	11835	This work
acetone	13.87	85.83	150	12874	This work
propionaldehyde	12.98	115.64	129	14917	This work
butyraldehyde	13.58	99.38	173	17273	This work
tetramethylethylenediamine	10.38	85.53	175	14967	This work
1,3-butanediol	5.51	55.92	238	13309	This work
n-butylamine	10.56	90.43	126	11394	This work

Extended Data Table 2 | Comparison of ΔS_{rev}, ΔT_{ad}, COP and relative Carnot efficiency (COP/COP_{Carnot}) for liquid-state barocaloric (n-hexane and ethyl acetate), typical solid-state caloric, polar-caloric and dissolution-based barocaloric refrigerants. The cold reservoir and heat sink temperatures are set to 300 and 308 K, respectively.

		Material	ΔS_{rev} (J/kg K)	ΔT_{ad} (K)	COP	COP/COP_{Carnot}	ref
solids	magnetocaloric	Gd	10	12	26.9	0.72	7
	elastocaloric	NiTi	27.3	13.8	19.6	0.52	7
	electrocaloric	DMHD-modified P(VDF-TrFE-CFE)	100	12	27.4	0.73	7
	barocaloric	$(DA)_2MnCl_4$	230	16.7	8.8	0.19	7
liquids	dipolar-caloric	KNO_3	390	18.6	24	0.9	9
	dissolution-BC	NH_4SCN aqueous solution	224	26.8	28.8	0.77	7
	barocaloric	n-hexane	232(246)†	31.3	37.5	~1	This work
	barocaloric	ethyl acetate	193(205)†	31.1	37.5	~1	This work

†The values are experimental data, while those in the brackets are from MD calculations.

34. Tao, K. et al. Giant reversible barocaloric effect with low hysteresis in antiperovskite $PdNMn_3$ compound. *Scripta Mater.* **203**, 114049 (2021).
35. Lin, J. et al. Giant room-temperature barocaloric effect at the electronic phase transition in $Ni_{1-x}Fe_xS$. *Mater. Horiz.* **7**, 2690-2695 (2020).
36. Yu, D., Richard, M. A., Terry, N. C., Shane, K. & Robért, R. Pelican — a Time of Flight Cold Neutron Polarization Analysis Spectrometer at OPAL. *J. Phys. Soc. Jpn.* **82** (2013).
37. Yuan, B. et al. Two Pressure Cells for Quasielastic and Inelastic Neutron Scatterings. *EPJ Web of Conferences* **272**, 02009 (2022).
38. Richard, D. et al. Analysis and visualisation of neutron-scattering data. *J. Neutr. Res*. **4**, 33-39 (1996).
39. S. Plimpton, P. C., A. Thompson. https://www.lammps.org/history (2007).
40. Siu, S. W., Pluhackova, K. & Bockmann, R.A. Optimization of the OPLS-AA Force Field for Long Hydrocarbons. *J. Chem. Theory. Comput.* **8**, 1459-1470 (2012).
41. Jorgensen, W. L. & Tirado-Rives, J. Potential energy functions for atomic-level simulations of water and organic and biomolecular systems. *Proc. Natl. Acad. Sci. USA* **102**, 6665-6670 (2005).
42. Dodda, L. S., Vilseck, J. Z., Tirado-Rives, J. & Jorgensen, W. L. 1.14* CM1A-LBCC: Localized Bond-Charge Corrected CM1A Charges for Condensed-Phase Simulations. *J. Phys. Chem. B* **121**, 3864-3870 (2017).

43. Dodda, L. S., Cabeza de Vaca, I., Tirado-Rives, J. & Jorgensen, W.L. LigParGen web server: an automatic OPLS-AA parameter generator for organic ligands. *Nucleic. Acids. Res.* **45**, W331-W336 (2017).
44. Padua, A. fftool v1.0.0 (v1.0.0). https://zenodo.org/records/18618 (2015).
45. Martinez, L., Andrade, R., Birgin, E.G. & Martinez, J.M. PACKMOL: a package for building initial configurations for molecular dynamics simulations. *J. Comput. Chem.* **30**, 2157-2164 (2009).
46. Perdew, J.P., Burke, K. & Ernzerhof, M. Generalized Gradient Approximation Made Simple. *Phys. Rev. Lett.* **77**, 3865-3868 (1996).
47. Tkatchenko, A. & Scheffler, M. Accurate molecular van der Waals interactions from ground-state electron density and free-atom reference data. *Phys. Rev. Lett.* **102**, 073005 (2009).
48. Zeng, M. et al. Colossal Reversible Barocaloric Effects in a Plastic Crystal Mediated by Lattice Vibrations and Ion Diffusion. *Adv. Sci.* **11**, 2306488 (2024).

Supplementary Files

This is a list of supplementary files associated with this preprint. Click to download.

- Supporting20260824.docx